Microwave-enhanced photovoltaic quantum oscillations of Weyl fermions

Jian-Feng Zhang,[1] Xiao-Wei Zhang,[1] Xiaohu Zheng,[1] Haiwen Liu,[2] Jian Mi,[3,1] Zhujun Yuan,[1] Shuang Jia,[1,4] X. C. Xie,[1,4] and Chi Zhang[5,6,1,4,*]

[1]*International Center for Quantum Materials, Peking University, Beijing 100871, China*
[2]*Department of Physics, Beijing Normal University, Beijing 100871, China*
[3]*Nanjing Research Institute of Electronic Technology, Nanjing, 210039, China*
[4]*Collaborative Innovation Center of Quantum Matter, Beijing 100871, China*
[5]*SKLSM, Institute of Semiconductors, Chinese Academy of Science, P.O. Box 912, Beijing 100083, China*
[6]*CAS Center for Excellence in Topological Quantum Computation, University of Chinese Academy of Sciences, Beijing 100190, China*

(Received 7 May 2020; accepted 23 October 2020; published 12 November 2020)

We perform magnetotransport and microwave (MW) photovoltage (PV) measurements in bulk tantalum arsenide (TaAs) crystal with c-(001) crystalline surface at low temperature (T). Two sets of quantum oscillations from different topological Weyl electron pockets are found in magnetoresistance and PV. Similar to the magnetoresistance, PV oscillates with the density of states around the Fermi level. Our observation qualitatively countenances a model which holds that the PV oscillations originate from nonequilibrium chiral Weyl fermions. Moreover, as a probe for detecting local electron states, PV is proved to be more sensitive than magnetoresistances. Microwave photovoltaic effect provides an effective method to explore topological electron structure and novel quantum phases in three-dimensional Weyl systems.

DOI: 10.1103/PhysRevB.102.205413

I. INTRODUCTION

Tantalum arsenide (TaAs), a member of Weyl semimetals (WSMs), is a three-dimensional (3D) topological matter. In the vicinity of band crossing points (i.e., Weyl nodes), electrons behave as massless Weyl fermions if the bands disperse linearly in momentum space [1]. Due to the nontrivial topology of Weyl fermions, Weyl semimetal exhibits novel quantum phenomena, such as Fermi arcs on the surface [2,3], and chiral-anomaly-induced quantum transport [4,5]. The first principle calculation predicts the existence of a dozen pairs of Weyl nodes in the Brillouin zone, including four pairs of Weyl nodes 1 (W1 at $k_z = 0$) and eight pairs of Weyl nodes 2 (W2 at $k_z = 0.592\pi$) [6]. Recent studies report strong anisotropy of W1 pockets, which is illustrated by experimental angular-dependent quantum oscillations (QOs) and Fermi surface (FS) calculation [7,8].

Photovoltaic effect triggered by circular polarized infrared light is currently employed to study the chirality of Weyl fermions in both theories and experiments [9–14]. But microwave (MW)-induced photovoltaic effect of nonequilibrium carriers has not been experimentally studied in WSMs. MW irradiation on high mobility two-dimensional electron (or hole) systems produces a wide range of phenomena [15–18]. This paper reports MW-enhanced photovoltaic Shubnikov-de Haas (SdH) oscillations in high mobility TaAs samples. From the magnetoresistance oscillations and the first principle calculation, we propose that the photovoltaic oscillations are induced by the nonequilibrium electrons of Weyl pockets. The MW power- and temperature-dependent PVs are consistent with those in nonequilibrium state model [19].

II. METHOD AND RESULTS: MAGNETOTRANSPORT

Our large-size high quality TaAs single crystals with (001) crystalline orientation are obtained via chemical vapor transfer (CVT) by using SnI_4 as the agent [20], which are then polished into rectangle samples. All measurements are performed in a dilution refrigerator (DR) with a base temperature (T) of 10 mK. We conduct four-terminal electric-transport studies with the delta measurement technique by a high-resolution electronic source/meter group.

To depict the Fermi pocket, we calculate the band structure and the FS based on the *ab initio* density functional theory. The band structure and the FS are obtained by utilizing the Vienna *ab initio* simulation package [21,22] through the WANNIER90 code [23]. The projected augmented wave (PAW) [24,25] potential and the Perdew-Burke-Ernzerhof [26] functional are included. An accurate electronic structure, including the spin-orbit coupling (SOC), is derived from the modified Becke-Johnson method [27,28], which has optimized the lattice constants and atomic positions.

We conduct magnetotransport measurements on TaAs samples. Figure 1(a) presents the longitudinal resistance and Hall resistance in a perpendicular B at 60 mK. At low B field [shown in the inset of Fig. 1(a)], the nonmonotonous behavior of R_{xy} provides evidence for the presence of both electrons and holes, which indicates that the Fermi level is close to the Weyl nodes. We adopt a two-band model on the basis of the Boltzmann equation to fit the electrical transport data at $B < 1$ T. In the model, the longitudinal and Hall conductivities are

*zhangchi@semi.ac.cn

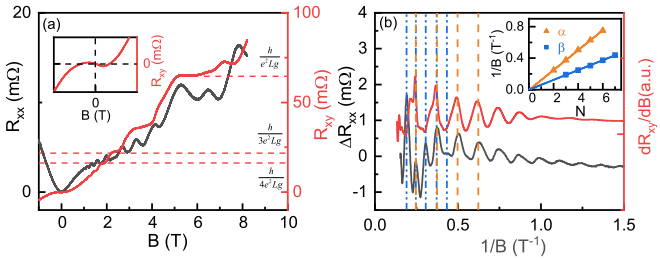

FIG. 1. (a) The longitudinal resistance (black) and Hall resistance (red) of the sample ($1.4 \times 1.2 \times 0.5$ mm^3) measured at 60 mK. The red dashed lines denote quantized values at about h/Ne^2Lg. Inset: the zoomed-in R_{xy} at low B (-0.2 T $< B <$ 0.2 T). (b) Comparison between the relative amplitude of R_{xx} (black) and the derivation of R_{xy} (red). The maxima of different frequencies are marked by orange dashed lines (α) and blue dash-dotted lines (β), respectively. The peaks of dR_{xy}/dB only appear at the maxima of the SdH oscillations from W1, as the orange dashed lines indicate. The inset of panel (b) displays $1/B$ versus LL index N of W1, W2.

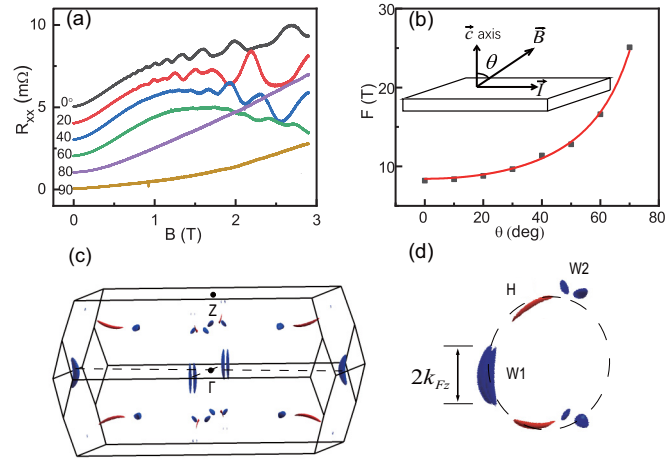

FIG. 2. (a) R_{xx} under tilted B ($\theta \sim 0$–$90°$). The traces are each offset by 1 mΩ for clarity. (b) Angular-dependent quantum oscillation frequencies. The black dots represent the frequencies obtained from the QOs in R_{xx}, and the red solid curve is the best fitting that follows the form of $F(\theta) \sim 1/\cos(\theta)$. (c),(d) First Brillouin zone and Fermi surface topology of TaAs according to the angular dependence in panel (a) at a Fermi energy of +8.5 meV.

derived as:

$$\sigma_{xx} = en_h\mu_h \frac{1}{1+(\mu_h B)^2} + en_e\mu_e \frac{1}{1+(\mu_e B)^2} \qquad (1)$$

and

$$\sigma_{xy} = \left[n_h\mu_h^2 \frac{1}{1+(\mu_h B)^2} - n_e\mu_e^2 \frac{1}{1+(\mu_e B)^2} \right] eB, \qquad (2)$$

respectively [20].

Through data analysis with the method in Refs. [20,29], we obtain the electron density $n_e = 9.3 \times 10^{17}$ cm^{-3}, the hole density $n_h = 1.0 \times 10^{17}$ cm^{-3}, the electron transport mobility $\mu_e = 6.0 \times 10^5$ cm^2/Vs, and the hole transport mobility $\mu_h = 5.8 \times 10^4$ cm^2/Vs, in the same order as in previous reports [7,20]. Owing to the high electron mobility, the electrons dominate the quantum transport at high B, whereas the hole contribution is negligible. At high B fields, two sets of QOs are observed, with the frequencies of $F_\alpha = 8.2$ T and $F_\beta = 16.5$ T, obtained from the fast Fourier transform (FFT) analysis. We distinguish the QOs from the two Weyl pockets of W1(α) and W2 (β) [7]. The R_{xy} traces display quantized plateaus (at h/Ne^2Lg) accompanied by oscillations with R_{xx}, as shown with the red dashed lines in Fig. 1(a), where N is the Landau level (LL) index. The degeneracy of $g = 4$ is due to the fourfold rotation symmetry in TaAs, and L is the quantum layer (QL) number in our bulk samples. We account for the phenomenon by the quantized plateaus of quasi-2D electron pockets W1, similar to the quantum Hall effects superposed in staked 2D systems [30–32]. Such phenomena have not been reported in previous experiments on TaAs to our knowledge.

The oscillatory spectrum in R_{xx} is complex because TaAs is a semimetal with multiple conductive channels [4]. For expository purpose, we display the quantum oscillations by subtracting a fourth-order polynomial background in Fig. 1(b), where the two SdH oscillations are indicated by the orange and the blue dashed lines. We compare the derivation of R_{xy} with the delta R_{xx} to reveal the origin of the plateau of R_{xy}. A key observation is that the peaks of dR_{xy}/dB and the signature of the R_{xy} plateaus only appear at the maxima of the SdH oscillations from W1. Therefore, we conclude that the plateaus of R_{xy} originate from W1.

In the transport of an electron pocket in a bulk, R_{xx} is expressed as: $R_{xx} = R_0[1 + A(B,T)\cos 2\pi(B_F/B - \gamma + \delta)]$ [33], where B_F is the SdH frequency, $\gamma = \frac{1}{2} - \frac{\phi_B}{2\pi}$ is the Onsager phase factor, with $\gamma = 0, 1$ (or $\gamma = \frac{1}{2}$) for the nontrivial (or trivial) Berry's phase ϕ_B, and δ denotes the phase shift which is determined by dimensionality, with $\delta = 0$ (or $\delta = \pm\frac{1}{8}$) for 2D (or 3D) systems. In order to elucidate the Berry's phase, we show the relation between $1/B$ and the LL index N in the inset of Fig. 1(b). The interpolation line of N versus $1/B$ illustrates $(\delta - \gamma)$ at 0.03 (for α) and at -0.10 (for β), respectively, which provides distinct evidence for the existence of the nontrivial π-Berry's phase arising from the Weyl electron pockets. The values of $|\delta|$ for α indicate the deviation of δ from the 3D limit $|\delta| = 1/8$, as a result of the quasi-2D nature of the W1 pockets. Meanwhile, the proximity of δ to 1/8 for β suggests a 3D property of W2 pockets.

To illustrate the chemical potential relative to the Weyl nodes, we study the angular-dependent magnetoresistance and the band structure of TaAs. Figure 2(a) presents R_{xx} at 60 mK by tilting B at an angle (θ) relative to the sample surface, as shown in the inset of Fig. 2(b). At small angles, the SdH oscillations are very robust. With increasing angles the oscillations gradually weaken and finally disappear at $\theta \sim 80$–$90°$. According to the features of W1 and W2 [see Figs. 1(a) and 1(b)], W1 electrons dominate the quantum transport under low magnetic field ($B < 3$ T). In Fig. 2(b), the angular-dependent QO frequencies express the relation $F(\theta) = 8.3/\cos(\theta)$ T, which confirms the quasi-2D property of W1 electron pockets. Due to the limit of the rotating magnetic field in our equipment, the high frequency (β) QOs are out of range for detection.

We have reconstructed the band structure by tuning Fermi energy E_F to +8.5 meV. The obtained contour of the Fermi

surface in three-dimensional k space is exhibited in Figs. 2(c) and 2(d), and the FS in the first Brillouin zone is illustrated in Fig. 2(c). The calculated frequencies ($F_\alpha = 8.31$ T and $F_\beta = 16.22$ T) are consistent with the experimental QO frequencies of W1, W2 ($F_\alpha = 8.3$ T, $F_\beta = 16.5$ T) at $E_F = 8.5$ meV. The energy is in the window phase so that the FS encloses individual Weyl points [8]. The FS is composed of one W1 pair, two W2 pairs, and two hole pockets, aligned along the nodal ring, as is shown by the FS topology in Fig. 2(d). The pea-shaped W2 pockets indicate that W2 is not strongly anisotropic. The banana-shaped W1 pockets at the zone boundary, which are aligned parallel to the c axis, give rise to the strong anisotropy and the 2D-like angular-dependent QOs.

Due to the strong anisotropy in k space, the W1 electrons are confined along the z-axis direction and can be defined as a quantum layer (QL). From the band structure, we obtain the Fermi wave vector $2k_{F,z} = 0.124$ Å, and the thickness of a single QL $\lambda_Q = \lambda_{F,z}/2 = 2\pi/2k_{F,z} = 5.0$ nm (half of the Fermi wavelength) [34], on the basis of which we estimate the number of QLs $L = \frac{d_{\text{sample}}}{\lambda_Q}$ (d_{sample}: sample thickness) and calculate the quantized values (h/Ne^2Lg). But by now, there has been little evidence for the lattice length of 5 nm in the normal direction of TaAs crystals. The mechanism to develop stacked 2D quantum Hall states in TaAs awaits further research.

III. METHOD AND RESULTS: PHOTOVOLTAIC MEASUREMENTS

Optical probing is another type of efficient tool to study Weyl fermions. We carry out the MW photovoltaic effect measurements by chopping the MW radiation at 391 Hz and detecting the voltage drop of two contacts at the chop frequency [17], as shown in Fig. 3(a). Different from other optical experiments on TaAs which utilize polarized infrared light on the chiral fermions [9,11], we conduct the MW photovoltaic detections on the states in nonequilibrium. The MW study of traditional 2DEG is from the view of transition between energy levels by absorbing photon energies [35]. In high B regime, when the cyclotron resonance energy $\hbar\omega_C = heB/m^*$ is larger than the photon energy, the transitions are prohibited. But with the multiple Landau bands near the FS of TaAs, the photoexcitation induces nonequilibrium carriers and generates giant PV at high B.

The experimental setup for the PV and the photocurrent (I_{ph}) study at low T is displayed in Fig. 3(a). The PV measurements are performed by chopping the MW radiation at 391 Hz and detecting the voltage drop of two contacts on the van der Pauw sample at the chopping frequency with a lock-in amplifier. The photocurrent is measured by the voltage drop across a load resistor ($R_L \sim 500\ \Omega$). The photovoltaic measurements are conducted without external current applied to the samples. The MW signal is guided down to the base via a coaxial cable, radiating the sample with a dipole antenna, which is perpendicular to the sample surface.

Figure 3(b) displays the photocurrent and the PV (at $f = 13$ GHz/$P = 15$ dBm) under perpendicular B, whose traces are identical, and exhibit strong oscillations, indicating the variation of density of states (DOS) near the Fermi level. The sharp peaks and valleys in the oscillations resemble those

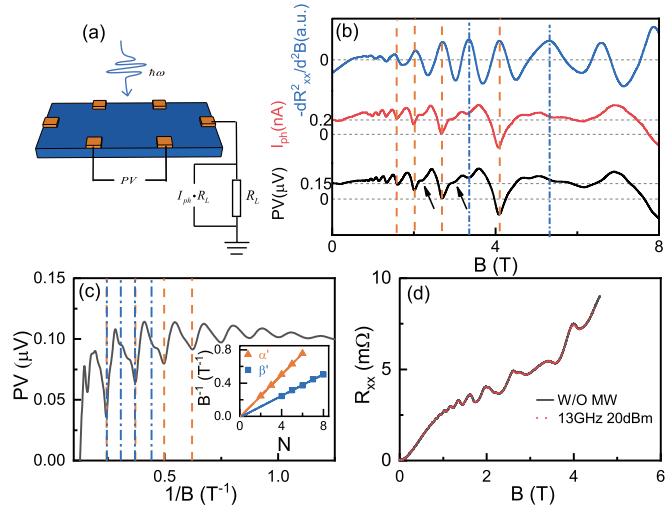

FIG. 3. (a) Schematic diagram of the photovoltaic measurement setup. $\hbar\omega$ denotes the microwave photon energy and the modulation frequency (f_{mod}) is 391 Hz. (b) Comparison between PV, I_{ph}, and $-d^2R_{xx}/dB^2$ (MW: $f = 13$ GHz, $P = 15$ dBm). The orange (blue) dashed lines indicate the contribution of W1 (W2) electron pockets, the valleys of PV and I_{ph} traces are aligned with the $-d^2R_{xx}/dB^2$ peaks. The black arrows point out the fine features of PV and I_{ph}. (c) Photovoltage versus $1/B$ is plotted. Two sets of SdH oscillations in PV are distinguished, and the minima of quantum oscillations are marked by orange dashed lines (α') and blue dash-dotted lines (β'), respectively. The inset shows the LL index of the two pockets. (d) Comparison of magnetoresistance with microwave off and on (13 GHz/20 dBm).

in magnetoresistance in ultrahigh mobility 2DES in GaAs [36]. In light of the similarity between the transport and the photovoltaic traces, we plot the negative second derivative of R_{xx} ($-d^2R_{xx}/dB^2$) [37] [the top curve in blue color in Fig. 3(b)] to reveal the mechanism of PV. At $B > 1$ T, as shown by the dashed lines (the orange dashed lines and the blue dot-dashed lines), the valleys of the photovoltaic traces are aligned with $-d^2R_{xx}/dB^2$ peaks. A fast Fourier analysis derives two frequencies of PV oscillations, $F_{\alpha'} = 8.2$ T and $F_{\beta'} = 16.0$ T, which are congruent with the results of R_{xx}. The two sets of SdH oscillations (α' and β') are identified in the measured PV signals [in Fig. 3(c)]. The fan diagram of the LL index is illustrated in the inset of Fig. 3(c), where we assign integer indices to the PV minima. The intercept of the N index ($\delta - \gamma$) is 0.07 for α' and 0.14 for β', in agreement with those in Fig. 1(c). Therefore, the minima in the photovoltaic traces are anticorrelated with the features in the magnetoresistance traces.

The photovoltaic effect results from two types of mechanisms: a built-in electric field and nonequilibrium electron states [19], both of which are induced by MW. The two mechanisms trigger the photovoltaic effect of TaAs. The Schottky component in the contacts induces a photodiode effect under MW radiation. The chemical potential difference between two contacts generates a built-in electric field, which leads to the diffusive electrons. Owing to the multiple Landau bands around FS, when the semimetal device is illuminated with MW radiation, carriers near the Fermi level absorb energy and

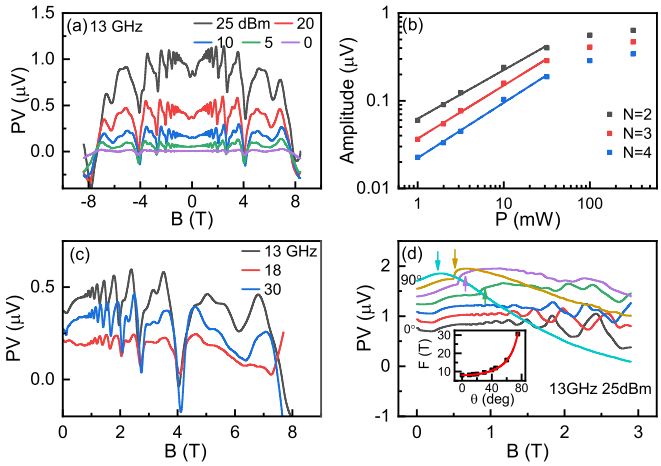

FIG. 4. (a) Power-dependent PV under B (at $f = 13$ GHz MW). The sample is kept at about $T = 0.2$ K. (b) The amplitudes of PV oscillations versus P for $N = 2, 3, 4$. The conventional unit mW is defined as $P(\text{dBm}) = 10\log_{10} P$ (mW), where $P(\text{dBm})/P(\text{mW})$ stands for power in the unit of dBm/mW. (c) Frequency-dependent PV under B at $T = 0.2$ K. (d) Angular-dependent PV ($\theta \sim 0, 15, 30, 45, 60, 75, 90^\circ$ from the bottom to the top curves), at 13 GHz/25 dBm MW. The arrows denote the phase shift of beatings under tilt. The traces are each offset by 0.2 μV for clarity. Inset: Angular-dependent QO frequencies. The black dots represent the frequencies determined by the PV oscillation under tilted B, and the red solid curve is the fitting of the angle-dependent frequencies: $F = 8.1/\cos(\theta)$ T.

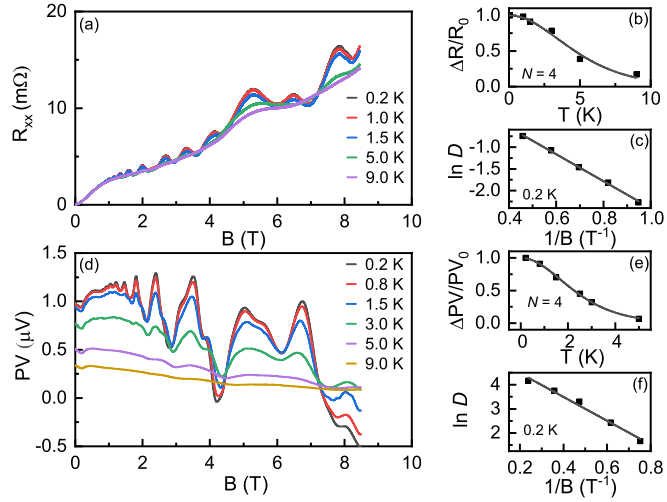

FIG. 5. (a),(d) T-dependent R_{xx} and PV under perpendicular magnetic fields. (b),(e) T-dependent amplitude of R_{xx} and PV at $N = 4$ for the cyclotron mass fitting. (c),(f) Dingle temperature plots for R_{xx}, PV at 0.2 K. The Dingle factor is expressed as $D = \Delta RB \sinh[\alpha T/\Delta E_N]$.

become mobile within a certain relaxation time. The mobile carrier drifting causes the photocurrent flowing between the contacts.

The voltage drop of PV has to do with the spatial separation of electrons and holes. I_{ph} and PV features are dependent on the mobility of the mobile carriers and the number of nonequilibrium carriers. As discussed in Fig. 1, the mobility of electrons is much higher than that of holes. Therefore, the nonequilibrium electron states dominate the photovoltaic effect. The number of nonequilibrium electrons is determined by the DOS in the vicinity of the Fermi level. By means of the nonequilibrium mechanism [19], the intensive QOs of I_{ph} and PV can be understood as the DOS oscillation of W1 electron pockets and W2 electron pockets under a perpendicular B. It can explain the correspondence of the valleys of photovoltaic traces with the peaks of $-d^2R_{xx}/dB^2$.

In addition, our observation rules out the local heating effect (e.g., the photo-Nernst effect). As shown in Fig. 3(d), in the comparison of the four-terminal transport measurements with and without MW, the two traces are identical. Moreover, the MW f- and sample T-dependent PVs are consistent with our nonequilibrium carrier transport model.

When the MW power is increased, the background value of PV grows as well ($f = 13$ GHz), as illustrated in Fig. 4(a). The PV traces are symmetric in relation to $B = 0$. Only the amplitudes of the PV oscillations substantially increase with the MW power. Figure 4(b) shows the relation between the oscillation's amplitude of each LL ($N = 2, 3, 4$) and the MW power (P) in logarithm of unit mW. In the low power region ($P < 15$ dBm), the amplitude of oscillations exhibits a linear response, which conforms to the photocurrent study of graphene [19,38]. The linear response breaks down at the power of 20 dBm, where the amplitude becomes saturated, as a result of the limitation of photoexcited electrons near FS.

The frequency-dependent measurement verifies the plausibility of the nonequilibrium carrier transport model, as demonstrated in Fig. 4(c). With the purpose to rule out the effect of f-dependent MW attenuations, the PV measurement is conducted at $T \sim 200$ mK by tuning the MW power. The observed QO features are f independent, which agrees with the mobile carrier model that the photoassisted hoppings are irrelevant to MW photon energy [19].

The quasi-2D property of W1 electron pockets is further confirmed by the angular-dependent PV under tilt [in Fig. 4(d)]. As has been discussed earlier, we only observe the PV oscillations of W1 electron pockets, due to the limitation of the tilted B. The inset of Fig. 4(d) shows the angular-dependent oscillating frequencies derived from the FFT analysis in PV. The frequencies at different angles exactly follow the $8.1/\cos(\theta)$ T rule, which is consistent with the angular-dependent R_{xx}. But distinct from the transport measurements, angle-dependent PV exhibits the phase shift of beatings, as highlighted by the arrows in Fig. 4(d). The phenomenon is attributable to interlayer hopping, which is studied in the transport of quasi-2D metals [39,40]. It also lends support to the QL model of W1 electron pockets.

With respect to the disparity of electron mobility between the transport and the PV, we analyze the T-dependent SdH oscillations in Figs. 5(a) and 5(d). The amplitude of ΔR_{xx} decreases with increasing T, and the oscillations are not observed above 9 K, which resembles PV oscillations. The magnetoresistance oscillations can be accounted for by the Lifshitz-Kosevich (L-K) formula:

$$\Delta R_{xx}(T, B) \propto \frac{\alpha T/\Delta E_N(B)}{\sinh[\alpha T/\Delta E_N(B)]}. \tag{3}$$

TABLE I. Summary of fitting parameters from R_{xx} and microwave PV oscillations.

	Frequency (T)	m^* (m_e)	T_D (K)	τ_q (ps)	μ_q (cm^2/Vs)
R_{xx}	8.2	0.184	3.2	0.38	3500
PV	8.2	0.192	1.8	0.70	6400

Given the similarity of the magnetoresistance and the PV features in Weyl semimetal, we analyze the PV oscillation as:

$$\Delta PV(T,B) \propto \frac{\alpha T/\Delta E_N(B)}{\sinh[\alpha T/\Delta E_N(B)]}, \tag{4}$$

in resemblance to the L-K formula (3), where $\Delta E_N(B)$ denotes the gap energy between the Nth and the $(N+1)$-th LL, and $\Delta E_N(B) = \hbar\frac{eB}{m^*}$. $T_D = h/(4\pi^2\tau_q k_B)$ represents the Dingle temperature, in which τ_q is the quantum lifetime and $\alpha = 2\pi^2 k_B$.

The quantum oscillations can be explained by virtue of the equation (4) at $B < 4$ T, where the features of W1 dominate, while the oscillations of W2 almost fade away. The effective mass m^* is obtained by fitting the T-dependent SdH amplitude damping, as shown in Figs. 5(b) and 5(e). τ_q and T_D are derived from the slope in the semilog plot of $D = \Delta RB\sinh[\alpha T/\Delta E_N]$ at $T = 0.2$ K in Figs. 5(c) and 5(f). All the fitting parameters are summarized in Table I. The effective mobility $\mu_q = e\tau_q/m^* = 6.4\times10^3$ cm^2/Vs is enhanced in PV measurements, which leads to the distinct SdH oscillations in PV.

IV. DISCUSSION

One of our findings is that the PV oscillations exhibit more fine features than magnetoresistance does, as highlighted by the black arrows in Fig. 3(b). Apart from the effect of MW-enhanced mobility, microwave mainly propagates along the "skin" of the conductive sample, which is referred to as the "skin effect." In our TaAs samples, the skin depth is estimated as: $d = \sqrt{\frac{1}{\omega\sigma\mu}} \sim 300$ nm. The PV detects the voltage drop of the nonequilibrium electrons on the skin of the samples, and the four-terminal measurement evaluates the summation of various conducting channels in the bulk samples. It can account for the MW-induced giant SdH oscillations in PV, but MW has no effect on the R_{xx} measurements [see Fig. 3(d)].

The origin of the robust photovoltaic effect in the bulk topological semimetals is very distinct from that of two-dimensional electron gas (2DEG) or regular metals. Our observation illustrates that the photovoltaic effect stems from MW induced built-in electric field and nonequilibrium states [19]. Although in noncentrosymmetric crystals photovoltaic effect could occur [i.e., the bulk photovoltaic effect (BPE)], piezoelectricity or ferroelectricity is required [41]. However, as a member of noncentrosymmetric material, TaAs has neither piezoelectricity nor ferroelectricity. Therefore, the mechanism of BPE can be ruled out.

In a 2DEG in HgTe-based semiconductor heterostructures, indiscernible photocurrent oscillations can be substantially enhanced by cyclotron resonance (CR) [42]. The phenomenon can be explained by a spin-dependent asymmetric energy relaxation: either the electron spin polarization under B fields or the difference in mobilities of spin-up and spin down electrons. But in our study of Weyl semimetal TaAs, the robust quantum oscillations in photovoltaic measurements are independent of CR, because the photovoltaic oscillations do not originate from the absorptions of CR energy. Moreover, the imbalance of electron and hole mobilities amplifies the oscillating features.

V. CONCLUSION

In summary, by means of magnetotransport measurements and the band structure calculation of TaAs, we have successfully illustrated the Fermi energy, which is located in the energy window phase for Weyl electron pockets. The distinct SdH oscillations in microwave PV originate from the nonequilibrium diffusive electrons in the Weyl pockets under photoexcitation. The photovoltaic effect on TaAs manifests variations of DOS under B fields, thereby providing an efficient tool to probe quantum states. In addition, the diffusive chiral fermions under MW excitations exhibit much higher mobility than the chiral fermions in equilibrium transport. The distinctive features of the MW photovoltaic effect of Weyl semimetals have great potential in the optoelectronic application of topological states, as the mobile Weyl fermions can be utilized to upgrade the quantum devices.

ACKNOWLEDGMENTS

We would like to thank Rui-Rui Du and Cheng-Long Zhang for the helpful discussion. This project is supported by the National Science Foundation of China (Grant No. 11674006, No. 11974339) and National Basic Research Program of China (Grant No. 2014CB920904). J.-F.Z. and C.Z. conducted the experiments; X.-W.Z. performed the calculation of the band structure and the FS; X.-H.Z., H.L., and X.-C.X. contributed to the discussion about the quantum transport, J.M. and C.Z. developed the microwave technique, J.-F.Z. and C.Z. analyzed data and wrote the paper, Z.Y. and S.J. grew the crystal samples, and C.Z. conceived and supervised the project.

[1] H. Weyl, Z. Phys. **56**, 330 (1929).
[2] X. Wan, A. M. Turner, A. Vishwanath, and S. Y. Savrasov, Phys. Rev. B **83**, 205101 (2011).
[3] G. Xu, H. Weng, Z. Wang, X. Dai, and Z. Fang, Phys. Rev. Lett. **107**, 186806 (2011).
[4] C.-L. Zhang, S. Y. Xu, I. Belopolski, Z. Yuan, Z. Lin, B. Tong, G. Bian, N. Alidoust, C. C. Lee, S. M. Huang, T. R. Chang, G. Chang, C. H. Hsu, H. T. Jeng, M. Neupane, D. S. Sanchez, H. Zheng, J. Wang, H. Lin, C. Zhang, H. Z. Lu, S. Q. Shen, T. Neupert, M. Z. Hasan, and S. Jia, Nat. Commun. **7**, 10735 (2016).
[5] S. A. Parameswaran, T. Grover, D. A. Abanin, D. A. Pesin, and A. Vishwanath, Phys. Rev. X **4**, 031035 (2014).

[6] H. Weng, C. Fang, Z. Fang, B. A. Bernevig, and X. Dai, Phys. Rev. X **5**, 011029 (2015).
[7] X. Huang, L. Zhao, Y. Long, P. Wang, D. Chen, Z. Yang, H. Liang, M. Xue, H. Weng, Z. Fang, X. Dai, and G. Chen, Phys. Rev. X, **5**, 031023 (2015).
[8] F. Arnold, M. Naumann, S.-C. Wu, Y. Sun, M. Schmidt, H. Borrmann, C. Felser, B. Yan, and E. Hassinger, Phys. Rev. Lett. **117**, 146401 (2016).
[9] Q. Ma, S. Y. Xu, C. K. Chan, C. L. Zhang, G. Chang, Y. Lin, W. Xie, T. Palacios, H. Lin, S. Jia, P. A. Lee, P. Jarillo-Herrero, and N. Gedik, Nat. Phys. **13**, 842 (2017).
[10] C. K. Chan, N. H. Lindner, G. Refael, and P. A. Lee, Phys. Rev. B **95**, 041104(R) (2017).
[11] Fernando de Juan, Adolfo G. Grushin, Takahiro Morimoto, and Joel E. Moore, Nat Commun. **8**, 15995 (2017).
[12] K. Taguchi, T. Imaeda, M. Sato, and Y. Tanaka, Phys. Rev. B **93**, 201202(R) (2016).
[13] Dmitri E. Kharzeev, Yuta Kikuchi, Rene Meyer, and Yuya Tanizaki, Phys. Rev. B **98**, 014305 (2018).
[14] L. E. Golub and E. L. Ivchenko, Phys. Rev. B **98**, 075305 (2018).
[15] M. A. Zudov, R. R. Du, J. A. Simmons, and J. L. Reno, Phys. Rev. B **64**, 201311(R) (2001).
[16] S. I. Dorozhkin, I. V. Pechenezhskiy, L. N. Pfeiffer, K. W. West, V. Umansky, K. von Klitzing, and J. H. Smet, Phys. Rev. Lett. **102**, 036602 (2009).
[17] J. Mi, J. Wang, L. N. Pfeiffer, K. W. West, K. W. Baldwin, and C. Zhang, Phys. Rev. B, **94**, 125411 (2016).
[18] Jian Mi, Huiying Liu, Junren Shi, L. N. Pfeiffer, K. W. West, K. W. Baldwin, Chi Zhang, Phys. Rev. B **100**, 235437 (2019).
[19] O. Gazzano, B. Cao, J. Hu, T. Huber, T. Grass, M. Gullans, D. Newell, M. Hafezi, and G. S. Solomon, arXiv:1903.01487.
[20] C.-L. Zhang, Z. Yuan, Q.-D. Jiang, B. Tong, C. Zhang, X. C. Xie, and S. Jia, Phys. Rev. B **95**, 085202 (2017).
[21] G. Kresse and J. Furthmülle, Comput. Mater. Sci. **6**, 15 (1996).
[22] G. Kresse and J. Furthmüller, Phys. Rev. B **54**, 11169 (1996).
[23] A. Mostofi, Comput. Phys. Commun. **178**, 685 (2008).
[24] P. E. Blöchl, Phys. Rev. B **50**, 17953 (1994).
[25] G. Kresse and D. Joubert, Phys. Rev. B **59**, 1758 (1999).
[26] J. P. Perdew, K. Burke, and M. Ernzerhof, Phys. Rev. Lett. **77**, 3865 (1996).
[27] A. Becke and E. Johnson, J. Chem. Phys. **124**, 221101 (2006).
[28] F. Tran and P. Blaha, Phys. Rev. Lett. **102**, 226401 (2009).
[29] Y. Ando, J. Phys. Soc. Jpn. **82**, 102001 (2013).
[30] B. I. Halperin, Jpn. J. Appl. Phys. **26**, 1913 (1987).
[31] H. L. Stormer, J. P. Eisenstein, A. C. Gossard, W. Wiegmann, and K. W. Baldwin, Phys. Rev. Lett. **56**, 85 (1986).
[32] H. Cao, J. Tian, I. Miotkowski, T. Shen, J. Hu, S. Qiao, and Y. P. Chen, Phys. Rev. Lett. **108**, 216803 (2012).
[33] H. Murakawa, M. S. Bahramy, M. Tokunaga, Y. Kohama, C. Bell, Y. Kaneko, N. Nagaosa, H. Y. Hwang, and Y. Tokura, Science **342**, 1490 (2013).
[34] F. Tang, Y. Ren, P. Wang, R. Zhong, J. Schneeloch, S. A. Yang, K. Yang, P. A. Lee, G. Gu, Z. Qiao, and L. Zhang, Nature (London) **569**, 537 (2019).
[35] R. L. Willett, L. N. Pfeiffer, and K. W. West, Phys. Rev. Lett. **93**, 026804 (2004).
[36] J. P. Eisentein and H. L. Stormer, Science **248**, 1510 (1990).
[37] P. T. Coleridge, R. Stoner, and R. Fletcher, Phys. Rev. B **39**, 1120 (1989).
[38] D. F. Karcher, A. V. Shchepetilnikov, Y. A. Nefyodov, J. Falson, I. A. Dmitriev, Y. Kozuka, D. Maryenko, A. Tsukazaki, S. I. Dorozhkin, I. V. Kukushkin, M. Kawasaki, and J. H. Smet, Phys. Rev. B **93**, 041410(R) (2016).
[39] P. D. Grigoriev, Phys. Rev. B **67**, 144401 (2003).
[40] P. D. Grigoriev, Phys. B: Condens. Matter **407**, 1932 (2012).
[41] V. M. Fridkin, Crystallogr. Rep. **46**, 654 (2001).
[42] C. Zoth, P. Olbrich, P. Vierling, K.-M. Dantscher, V. V. Bel'kov, M. A. Semina, M. M. Glazov, L. E. Golub, D. A. Kozlov, Z. D. Kvon, N. N. Mikhailov, S. A. Dvoretsky, and S. D. Ganichev, Phys. Rev. B **90**, 205415 (2014).